

Monitoring and Stability Evaluation of the Damaged Landslide Based on Multiple Monitoring Technologies

Wei Huang

Chongqing Engineering research center of automatic for geological

Chang Zhou (✉ changzhouc@cumt.edu.cn)

China University of Mining Technology: China University of Mining and Technology

Hong Xu

Chongqing engineering research center of automatic for geological hazards

Lichuan Chen

Chongqing Engineering Research center of automatic for geological hazards

Yunping Liao

Chongqing Engineering research center of automatic for geological hazards

Pengfei Liu

Chongqing Institute of geological environment monitoring

Yaohui Gao

Zhejiang University of Technology

Research Article

Keywords: Damaged landslide, Emergency monitoring, Rainfall, Failure mechanism, Thermal infrared temperature

Posted Date: March 29th, 2021

DOI: <https://doi.org/10.21203/rs.3.rs-349281/v1>

License: © ⓘ This work is licensed under a Creative Commons Attribution 4.0 International License.

[Read Full License](#)

Abstract

The stability evaluation of the damaged landslide is important for rescue work and emergency operation. This paper investigated a predisposing geological emergence, inducing the factors and deformation processes of the Zhongbao landslide, which happened on 25 July 2020. The stability of the damaged landslide was evaluated by an integrated monitoring system consisting of ground-based radar, unmanned aerial vehicles, airborne Lidar, thermal infrared temperature monitoring, GNSS displacement monitoring, deep displacement monitoring and rainfall monitoring. The strata and weak layer controlled the landslide failure, and topography defined the boundary of the failed rock mass. A continually intensive rainfall caused the deformation and accelerated failure of the landslide. The shallow and steep deposit (Part I) firstly slid at a high velocity, and then pushed the rear part of the landslide (Part II) to deform, forming numerous cracks, and the rainfall infiltrated into the rock mass. Finally, the rock and soil mass sliding along the weak layer, a barrier dam and a barrier lake were formed. The monitoring results showed that after the landslide failure, there were still local collapse and deformation occurrence which threatened rescue work and barrier lake excavation. Therefore, the barrier dam wasn't excavated until the accumulation rate gradually stabilized on July 28. Moreover, most of the reactivated deposits still accumulated in the transportation and source areas. Thus, in August, the displacement of the damaged landslide gradually accelerated in a stepwise manner, and responded strongly to rainfall, especially in the accumulation area, so that it was inferred that the damaged landslide could slide again and caused a more threatening and severe failure. The analysis results of the study area can provide references for the failure mechanism of a rainfall-induced landslide and the stability evaluation of a damaged landslide.

Introduction

Rainfall-induced landslides are widely distributed in the world, for example over 2500 landslides events were reported between 1950 to 2005 (Fausto et al., 2008). Rainfall intensifies landslide material, and groundwater level change could cause the dynamic and static pore pressure inside landslide masses (Vita et al. 1998; Tsai 2008; Li et al., 2018). As one of the most catastrophic and destructive types of landslides, the consequent bedding rock has strong sensibility to water, because the weak structural layer is widely developed in rock strata (Gu, 1979; Huang, 2007; Yin, 2011; Tang et al., 2019), such as 2008 Jiweishan landslide (Yin et al., 2011; Tang et al., 2015; Zhang et al., 2018), 2006 Leyte landslide (Evans et al., 2007; Guthrie et al., 2009), Mashangwan landslide (Yin, 2010), and so on. Therefore, it is necessary to study the deformation characteristics and failure mechanism of consequent bedding rock slopes triggered by rainfall.

Multi-field information is very important in understanding the deformation characteristics of the landslide. Over the last decade, some new technologies have been developed to monitor landslide deformation, such as GB-InSAR, TLS, IRT and digital photogrammetry (DP) and so on (Ventisette et al., 2011; Bardi et al., 2014; Crosetto et al., 2016; Zin et al., 2016; Casagli et al., 2017; Li et al., 2020; Zhou et al., 2020), and achieved remarkable achievements in monitoring, prediction, early warning of the landslide (Lillesand et al., 2014; Xu et al., 2016; Piciullo et al., 2018; Ouyang et al., 2019). Those technologies are

characterized by more efficient operation and higher accuracy of monitoring data compared with traditional monitoring sensors: high-resolution image data acquisition, data diversity, device portability, easy and fast data processing (Casagli et al., 2017). Those devices could systematically and easily update the data. However, there are few reports about monitoring damaged landslides, where local deformations or collapse still occur and threaten rescue work and emergency work.

The catastrophic landslide occurred in Chongqing, China, during July 23 -27. 520 persons were evacuated and two roads were damaged. A barrier lake formed and threatened the safety of over 8,500 residents in the downstream Quantang Hydropower Station and Canggou Township (Chen et al., 2020). In this paper, a deformation process and failure model of landslides are analyzed by using some advanced technologies in the field of landslide mapping and monitoring for short term landslide management to provide information for the barrier lake excavation and the rescue work. After the damaged landslide was stable, some traditional methods were constructed in landslides, and the monitoring data was used to evaluate the stability of the deposit.

Materials And Methods

2.1 Description of the Zhongbao landslide

The Zhongbao landslide is located at the north side of the Yancang river, about 59 kilometers to the Wulong District, Chongqing, China (Fig.1 a). In plane view, the shape of the Zhongbao landslide approximately likes a tongue, with 850 m length and 200 m width (Fig.1 b). The thickness of the landslide is estimated 25m -47 m, and its' volume is approximately $4.6 \times 10^6 \text{ m}^3$ (Fig.1 c). The slope of the landslide surface is 25° - 45° . The main sliding direction is 210° , approximately perpendicular to Yancang River. The Zhongbao landslide began to slide at 16 p.m. July 23, 2020, and destroyed three buildings and main roads. Over $1.0 \times 10^4 \text{ m}^3$ soil and rock masses slipped into the river and formed a barrier lake.

The field investigation indicates that main geologic units of the area are deposits and shales. The uppermost part of the surficial deposits is eluvial deposits (up to 0.5~3.5 m thick), whereas stratigraphically lower layers comprise mostly alluvial deposits and colluvial deposits. The eluvial deposits consist of clay and 10% ~ 45% of gravel clasts (Fig. 2 a, b). The diameter of gravel clasts ranges from 50 mm to 300 mm. In-situ exposed outcrops over 10 m high (undisturbed by the landslide) crops out near the western limit of the depicts the lithological structure (Fig.2 c). Dominant pale-yellow shales, 0.2 m ~ 0.5 m thick, are in the pelitic structure with developed joints. The mainly component of shales are smectite and other clay minerals which are easy to be weathered and softened by water. The rocks dips 25° toward 130° . Three dominate joints are found in the study area (Fig. 2 d). The first joint dips 75° toward 351° with a width of 3~ 15 mm and a length of 1.5 – 4.9 m, and its space is 1.30 – 4.20 m. The second one is dips 84° toward 128° with a width of 2 -12 mm and a length of over 10 m, and its space is 1.10 -2.70 m. The third dips 76° toward 276° with a length of 2.1 – 4.5 m and its space is 0.80 -3.60 m. Those joints are partially filled with clay.

2.2 Landslide monitoring after failure

2.2.1 Emergency monitoring system

After landslide failure, emergency work and stability evaluation of the reactivated deposits are necessary, but conventional monitoring technologies are not equipped in monitoring the damaged landslide, because of the instability of the landslide. Therefore, some new methods are taken to monitor the deformation of the landslide(Figure 3):

(1) Ground-based radar

HC-GBSAR1000 ground-based radar monitoring system uses the Ground-based repeated orbit interferometric SAR technology, which accurately measures the displacement of the landslide's surface by comparing different pictures at different times based on the principle of phase interference. This technology has technical advantages of all-weather, high-precision, and continuous measurement in time and space. Therefore, it is used in emergency monitoring of the landslide.

(2) Unmanned Aerial Vehicle

Five sensors are equipped in the unmanned aerial vehicle to take pictures from five views. Meanwhile, the location of the vehicle during flying are recorded, including its height, speed and flying direction. Based on the digital aerial stereo images, the image points and coordinates are automatically recognized, and the three-dimensional coordinate of the study objection is formed by using analytical photogrammetry method. This technology could rapidly obtain a digital orthophoto, a digital elevation model, and high-resolution three-dimensional models, which provide fundamental data for the evaluation and monitoring of the landslide.

(3) Airborne Lidar

The airborne Lidar integrates multi-technologies, such as laser, computers, high dynamic carrier attitude determination technology and High-precision dynamic GNSS (Glogbal navigation satellite system) differential technology. This technology recognizes objects by laser technology, and analyzes those datum by computer technology. Airborne lidar is composed of a laser scanner system, a POS system (GNSS) and a high-resolution camera system. The technology can avoid the effect of trees and obtain a high-resolution photograph and 3D point cloud data rapidly and accurately. Those datum are used to analyze the deformation and the volume of the landslide.

(4) Thermal infrared temperature monitoring

The thermal Infrared Camera FLIR X8400sc is a device which converts energy into electrical signal. It has a precision of ± 0.1 °C, a temperature resolution of 0.04 °C, a resolution of 1280 × 1024 pixels and a spectral range of [1.5 5.1] m. This equipment measures the temperature of the landslide surface so as to obtain the temperature of the field.

2.2.2 Conventional monitoring system

Conventional monitoring equipment has been widely used in natural hazards monitoring because of their low cost, simple structure and easy construction. In addition, they are applied for its wireless transmission in measurement data. In this paper, those monitoring technologies are used (Fig. 3):

(1) GNSS displacement monitoring

The principle of GNSS monitoring is to determine the position of the GNSS receiver using distance intersection method by measuring the distance between four or more satellites and receivers. The base station is constructed in a stable area, and monitoring stations are built in a deformation area. The displacements of the monitoring stations are calculated by comparing the location between base and monitoring stations.

(2) Displacement monitoring in depth

The flexible inclinometer probe, invented by Chongqing Engineering Research Center of Automatic Monitoring for Geological Hazards, measured its angle by three-dimensional micro-mechatronics measurement units (MEMS) to calculate the horizontal displacement. The flexible probe monitoring system includes a flexible probe, controller and PC software. One probe contains 80 measurement units and a vertical spacing of 1.0 m.

(3) Rainfall monitoring

A tipping-bucket rain-gauge is used to measure precipitation, because it is characterized by real-time recording rainfall with high accuracy and almost without human factors. The measurable range of the equipment is 0.01 mm–4 mm/min, and the precision is $\pm 2\%$.

(4) Sound and light alarm

The received data being collected and analyzed by the monitoring terminal, is uploaded to the remote control terminal and then the alarm information is pushed to the sound and light warning terminal for efficient and timely warning. Sound and light alarms are carried out in time to remind nearby vehicles and personnel to react to disasters.

Results

3.1 Deformation of the Zhongbao landslide

The Zhongbao landslide was firstly found deformed on July 22. Several cracks were recorded at the uphill side of the landslide after a continues intense rainfall. As the landslide deformed, the east boundary of the landslide was generated, then a plenty of tension cracks formed at the Part II while Part I failed (Fig. 4b). The uphill slope slide over 20 m, but the downhill slope had local deformation. On July 24, the sliding mass was transported to the middle and downhill slope; downhill slope gradually failure

(Fig. 4 c). On July 25, there was a strong rainfall, the downslope had obvious deformation, and the sliding mass gradually slid into Yancang River. The barrier lake and bam were formed (Fig. 4d e).

The steep Part I firstly deformed and failed, which destroyed the main road. The upstream portion of Part II gradually deformed and pushed the middle portion to slip. Due to the cliff at the east side of the landslide, the sliding direction of the landslide gradually changed from 165° in the source area to 220° in the transportation area, and finally to 180° in the accumulation area. According to the deformation characteristics of the landslide, the landslide area could be divided into five areas (Figure 9):

Part I: This portion is located at the north-east side of the landslide (Fig. 5). Reactivated deposits of Part I covered Part II. This part is 140-245 m wide and 230 m long, about 10 m thick with a highest elevation difference of 102 m. The deformation characteristics of the road showed that the accumulation moved with Part II, inferred that Part I failed before Part II. Due to the steep slope, engineering projection and continual rainfall, Part I slipped with velocity and compressed Part II which accelerated the movement of Part II. Therefore, the uplift area and puddle were found in the part II.

Source area (Fig. 5): The length and elevation difference of this area is approximately 207 m and 46 m, respectively. Under the effect of rainfall and part I, the rear section of Part II gradually deformed and developed into scratch (Fig. 6 a) and tension cracks. Those cracks became an infiltration path for rainfall which damaged the yale structure and decreased the shear strength of the soil and rock. The rock became severely fragmented (Fig. 6 b). The deformation of the landslide accelerated. Many scarplets and cracks were found in this portion. Moreover, the boundary between the source area and the transportation area was an uplift zone with an average height of 3.0 m (Fig. 5).

Transportation area (Fig. 7): Owing to the rear section sliding and pushing the rock soil mass in the transportation area, some buildings and houses in the middle section only formed tension cracks but not completely destroyed (Fig. 7). Some parts were uplifted. In plane view, this area had an approximately rectangular shape with a length of 340 m and an average width of 175 m. Some pools were found on the landslide. the road debris showed that it slid about 99 m but kept good continuity.

Accumulation area (Figure 8): The rear part became steep again, and the dip direction of the exposed rock was 15° . Thus, the sliding direction of the landslide changed. The sliding mass slip and mobilized surficial deposits in the accumulation area by scraping, entraining, and pushing them downward. Finally, the reactivated deposits accumulated in the toe of landslide and formed a barrier dam and barrier lake. The thermal infrared monitoring found that the temperature field appeared abnormal in the place where the groundwater was exposed. Moreover, the temperatures of the accumulation area were higher than other area.

Secondary -landslide area: Three secondary-landslide (1-3# in Figure 9) were found at the west side of the landslide because of the V-shaped valley. No.1 secondary-landslide is caused by the source area sliding along the direction of 230° . No.2 is located on the cliff, so it could be the collapse of the sliding mass. No. 3, caused by the change of the sliding direction of Part II, occurred and buried a small road.

3.2 Stability of the failure landslide

(1) Visual observation of surface deformation

The radar technology was used to evaluate the volume and deformation characteristics of the landslide, because it can remove the trees on the landslide surface and obtain the rear geography of the landslide. Figure 9 shows that the Part I had an obvious boundary with $4.1 \times 10^2 \text{ m}^2$. Its' sliding mass accumulated in the Part II and slipped to the transportation area of the Part II. The downhill slope continued to progressive retrogressive collapse and slid into river. Thus, this landslide is still unstable. Moreover, a cliff was observed on the northeast side of the landslide with over $1 \times 10^6 \text{ m}^2$ colluvial deposits where was also the occurrence of Part I.

(2) Surface displacement

An emergency monitoring was started from July 27 to Aug 2. Ground-based radar was 2.8 km away from the landslide (Fig. 3). The surface deformation of the landslide was scanned from July 27 to October 2. Unfortunately, the monitoring is un-continuous due to the power issues and the change of the device location. Therefore, two periods are selected to analysis the deformation characteristics of the failure landslide.

Figure 10 is the monitoring results of the landslide surface from 16:00 pm July 27 to 6: 00 am July 28. The uphill and middle of the landslide has no obvious deformation, but the downhill section has large deformation with largest displacement of 200 mm (Fig. 10a). The displacements of four monitoring points in the downslope are shown in Figure 10b. It is observed that the displacement of P2 and P4 slowly increased and reached about 50 mm. However, the displacement at P1 and P3 had the largest values. The velocity of P1 gradually decreased after July 28. The displacement at P3 sharply increased at 22:00 July 27 and then tend to stable. Moreover, local deformation was also found at the cliff on the northeast side of the downslope (approximately -50 mm).

Figure 11 shows the displacement of the landslide surface from 11:00 am to 5:00 pm July 28. It was found that the largest displacement of the landslide is about 70 mm, which is obvious smaller than that in Figure 10 (Figure 11 a). The displacement of the point at P was monitored (Figure 11 b). The displacement increases with a velocity of 12 mm/h, which indicated that the local collapse still occurred. Figure 11 c shows that the upslope also had small deformation (>40 mm) and the whole landslide was stable.

In consequence, after the landslide failed, this landslide tends to stable except local collapse. The emergency works were taken in the source and transportation area before July 28, and then, the barrier dam was excavated on July 28. The traditional monitoring equipment were installed in the landslide surface.

In Fig. 12, the rainfall and displacement from Aug 12 to Oct 1 were recorded. The second wet month (from September to October) was characterized by a 333 mm cumulative rainfall. The downhill slope (G05, G06) had large deformation with a velocity as high as 6 cm/day (G06). The increment displacement of the G06 suddenly decreased tending to zero, but the G05 went on with a constant rate of 3.8 mm/day. Clearly, the rainfall reactivated the landslide. Moreover, the increase of the displacement at G06 and G05 generally lagged 1 day behind the rainfall. Other portion of the landslide had small displacement (<30 mm /month), but also responded to the rainfall and gradually increased.

Discussion

4.1 Failure mechanism of the Zhongbao landslide

Water has a significant effect on the strength of the shale rock. The increase of the water content could lead to the mineral particle dissolution and the increase of the clay mineral. As results, the shale structure become loose, the mic-cracks gradually increase, and finally, the rock degrades and softens (Zhu et al., 2015; Feng et al., 2005; Cornelius et al., 2011; Ling et al., 2016; Liu et al., 2016; Xue et al., 2018; Li et al., 2019). Moreover, field investigation found that the primary porosity of shale in the landslide area was well developed, and three sets of the superior fractures caused the loose of the rock. Therefore, after a constant rainfall (July 15-18), the rainfall infiltrated into the landslide and decreased the shear strength of the rock. Further, underground water had lubrication effect on the rock layers, so that the landslide began to deform at July 22. The displacement of the monitoring results also showed that the failure landslide had a large deformation after a strong rainfall (Sep 6). Moreover, the lag time of the landslide deformation after failure (about 1 day) was shorter than that of the landslide before failure response to rainfall (about six days), which could because the loose deposits after landslide failure accelerated the rainfall infiltration. According to the deformation characteristics of the landslide, the deformation process could be divided into four stage:

Creep deformation stage: Rainfall caused shallow landslide (Part I). The reactivated deposit impacted and compressed the upslope of the part II which accelerated the deformation of the landslide. Thus, the scratch and shear cracks were generated at the uphill side of the landslide (Figure 6). The uphill section gradually generated obvious deformation. The deformation direction of part I is 230°.

Accelerated deformation stage: After the rear part of the landslide was initiated, it gradually slid along the sliding zone and compress the middle section. The sliding zone rapidly develop and the landslide slides over 90 m. The sliding direction is 210°.

Accumulation stage: the landslide slides out from the steep ridge of the front edge and pushes and scrapes the shale, which accumulates at the foot of the landslide and a barrier lake is formed. Moreover, the scarplet in front of the landslide led to the deposit mainly accumulate in the landslide toe and formed a secondary landslide (Figure 9) which still deformed after the landslide failure, especially when heavy rainfall occurs.

4.2 Emergency monitoring system for the damaged landslide

After landslide failure, the re-activated deposit and the barrier lake could cause secondary economic losses, so that the emergency engineering is necessary. However, under the effect of earthquake and rainfall, the second landslide or collapse could occur and threat people's lives and their economic safety. This paper constructed an integrated monitoring system for landslide failure. The monitoring equipment is non-contact measurement such as Ground-based radar, Unmanned Aerial Vehicle, Airborne Lidar, and thermal infrared temperature monitoring. Those devices can scan the whole landslide surface and obtain point cloud data to evaluate the stability of the failure landslide in detail. The monitoring results found that deformation mainly occurred in the scarp at the uphill side of the landslide, and the deformation gradually tend to be stable after July 28. Those results provided guidance for rescue work and the excavation of barrier lakes. However, those devices are too expensive and difficult to operate if used for long-term monitoring of landslides, and they also only obtain deformation information of the landslide surface. Therefore, After the failure landslide gradually stable, the conventional sensors should be installed into the landslide to measure the displacement of the typical landslide profiles, such as GNSS, GPS, deep monitoring and so on. Those devices can measure the multi-filed information of the landslide for a long time without interruption, which could provide information for the reconstruction work. In this paper, the monitoring for the failure landslide shows that the failure landslide still response to the rainfall, especially at the front and middle part of the landslide. Thus, the engineering activities and human activities should be avoided as far as possible in the middle and front part for the landslide could slide again and form a dammed lake. Moreover, over 1×10^6 m² colluvial deposits on the northeast side of the landslide could be initialed and fail under a long-term effect of rainfall, which could cause an extensive damage of the landslide.

Conclusion

The Zhongbao landslide is a typical rainfall-induced landslide in the Yancang River, situated on the Wulong District, Chongqing, China. It most likely originated catastrophically as a rockslide combined with a shallow landslide. The shallow soil slope, located in the uphill side of the landslide was triggered by a continuous torrential, which pushed the rear part of the landslide to deform and rainfall accelerated infiltrated into the landslide. The increase of the water content decreased the strength of the shale rock and made the brock rock more broken. The landslide gradually slid along the weak layer within the rock layer and formed a barrier lake. Moreover, the accumulation area was still deformed.

After the landslide failure, an emergency monitoring system with multiple monitoring devices was constructed to measure the deformation of the whole landslide surface. The monitoring results provided some advices for the emergency engineering. The failure landslide was gradually stable after July 28. Then some conventional monitoring methods were installed into the landslide and the results found that the reactivated deposits still responded to the rainfall.

Declarations

Acknowledgments: This study was financially supported by the National Key Research and Development Program of China (Grant No. 2017YFC1501303); Chongqing Technology Innovation and Application Development Special Key Projects(cstc2019jscx-tjsbX0015). The authors appreciate the work of Chengdu University of Technology for providing the data of the thermal infrared temperature monitoring. All support is gratefully acknowledged.

References

1. Bardi FW, Frodella A, Ciampalini S, et al. Integration between ground based and satellite SAR data in landslide mapping: the San Fratello case study[J]. *Geomorphology*, 2014, 223: 45-60.
2. Casagli N, Frodella W, Morelli S, et al. Spaceborne, UAV and ground-based remote sensing techniques for landslide mapping, monitoring and early warning[J]. *Geoenvironmental Disasters*, 2017, 4: 1-23.
3. Chen LC, Yang HQ, Song KL. Failure mechanisms and characteristics of the Zhongbao landslide at Liujing village, Wulong, China[J]. *Landslides*, 2021.
4. Cornelius F, Stephan K, Wang JW, et al. Weathering of Fruchtschiefer building stones: mineral dissolution or rock disaggregation? [J]. *Environmental Earth Sciences*, 2011, 63: 7-8.
5. Crosetto MO, Monserrat M, Cuevas-González, et al. Persistent scatterer interferometry: a review[J]. *ISPRS Journal of Photogrammetry and Remote Sensing*, 2016, 115: 78-89.
6. Evans SG, Guthrie RH, Roberts NJ, et al. The disastrous 17 February 2006 rockslide-debris avalanche on Leyte Island, Philippines: a catastrophic landslide in tropical mountain terrain. *Natural Hazards and Earth System Sciences*, 2007, 7, 89-101.
7. Feng XT, Ding WX. Meso-mechanical experiment of micro-fracturing process of rock under coupled mechanical-hydrological chemical environment[J]. *Chinese Journal of Rock Mechanics and Engineering*, 2005, 24(9): 1465-1473.
8. Gu DZ. *Foundation of rock mass engineering geomechanics*[M]. Science Press, 1979, Beijing.
9. Guthrie RH, Evans SG, Catane SG, et al. The 17 February 2006 rock slide-debris avalanche at Guinsaigon Philippines: a synthesis. *Bulletin of Engineering Geology and the Environment*, 2009, 68: 201-213.
10. Huang RQ. Large-scale landslides and their sliding mechanisms in China since the 20th century[J]. *China Journal of Rock Mechanics Engineering*, 2007, 26:433-454.
11. Li YS, Jiao QS, Hu XH, Li ZL, et al. Detecting the slope movement after the 2018 Baige Landslides based on ground-based and space-borne radar observations[J]. *International Journal of Applied Earth Observation and Geoinformation*, 2020, 84: 1-12.
12. Li ZB, Huang TM, Pang ZH, et al. 2019. Study on groundwater baseline quality, monitoring indicators and contamination tracing methods related to shale gas development: a case study in the fulling gas field in SW China[J]. *Journal of Engineering Geology*, 27 (1): 170 - 177.
13. Li CR, Wang M, Liu K. A decadal evolution of landslides and debris flows after the Wenchuan earthquake[J]. *Geomorphology*, 2018, 323: 1-12.

14. Lillesand T, Kiefer RW, Chipman J. Remote sensing and image interpretation. Wiley, 2014, pp. 736.
15. Ling SX, Wu XY, Sun CW, et al. Experimental Study of Chemical Damage and Mechanical Deterioration of Black Shale Due to Water-Rock Chemical Action[J]. Journal of Experimental Mechanics, 2016, 31(4): 511-524.
16. Liu X, Zeng W, Liang L, et al. Experimental study on hydration damage mechanism of shale from the Longmaxi Formation in southern Sichuan Basin, China[J]. Petroleum, 2016, 2: 54-60.
17. Nicola C, Filippo C, Chiara DV, et al. Monitoring, prediction, and early warning using ground-based radar interferometry[J]. Landslides, 2010, 7:291-301.
18. Ouyang C, Zhao W, An H, et al. Early identification and dynamic processes of ridge-top rockslides: implications from the Su Village landslide in Suichang County, Zhejiang Province, China[J]. Landslides, 2019, 16:799-813.
19. Piciullo L, Calvello M, Cepeda JM. Territorial early warning systems for rainfall-induced landslides[J]. Earth-Science Reviews, 2018, 179:228-247.
20. Tang H, Zou Z, Xiong C, et al. An evolution model of large consequent bedding rockslides, with particular reference to the Jiweishan rockslide in Southwest China[J]. Engineering Geology, 2015, 186: 17-27.
21. Tang JX, Dai ZY, Wang YL, et al. Fracture Failure of Consequent Bedding Rock Slopes After Underground Mining in Mountainous Area[J]. Rock Mechanics and Rock Engineering, 2019, 52:2853-2870.
22. Tsai TL. The influence of rainstorm pattern on shallow landslide[J]. Environmental Geology, 2008, 53(7): 1563-1569.
23. Ventisette CD, Intrieri E, Luzi G, et al. Using ground based radar interferometry during emergency: the case of the A3 motorway (Calabria Region, Italy) threatened by a landslide[J]. Natural Hazards and Earth system Sciences, 2011, 11: 2483-2495.
24. Xu Q, Liu HX, Ran J, et al. Field monitoring of groundwater responses to heavy rainfalls and the early warning of the Kualiangzi landslide in Sichuan Basin, southwestern China[J]. Landslides, 2016, 13: 1555-1570.
25. Xue HQ, Zhou SW, Jiang YL, et al. Effects of hydration on the microstructure and physical properties of shale[J]. Petroleum Exploration and development, 2018, 45(6): 1075-1081.
26. Yin YP. Recent catastrophic landslides and mitigation in China[J]. Journal of Rock Mechanics and Geotechnical Engineering, 2011, 3:10-28.
27. Yin Y, Sun P, Zhang M, et al. Mechanism on apparent dip sliding of oblique inclined bedding rockslide at Jiweishan, Chongqing, China. Landslides, 2011, 8: 49-55.
28. Zhang M, Mauri M, Shao H, et al. The 2009 Jiweishan rock avalanche, Wulong, China: Precursor conditions and factors leading to failure[J]. Engineering Geology, 2018, 233:225-230.
29. Zhou C, Ying CY, Hu XL, et al. Thermal Infrared Imagery Integrated with Multi-Field Information for Characterization of Pile-Reinforced Landslide Deformation[J]. Sensors, 2020, 17: 1-7.

30. Zhu BL, Li XN, Wu XY, et al. Experimental study of micro-characteristics of selling for black shale under influence of water[J]. Chinese Journal of Rock Mechanics and Engineering, 2105, 34(Z2): 3896-3905.
31. Zin A, Hawari K, Khamisan N. Early Detection of Spots High Water Saturation for Landslide Prediction Using Thermal Imaging Analysis[J]. International Journal of Environmental Science and Development, 2016, 7(1): 41-45.

Figures

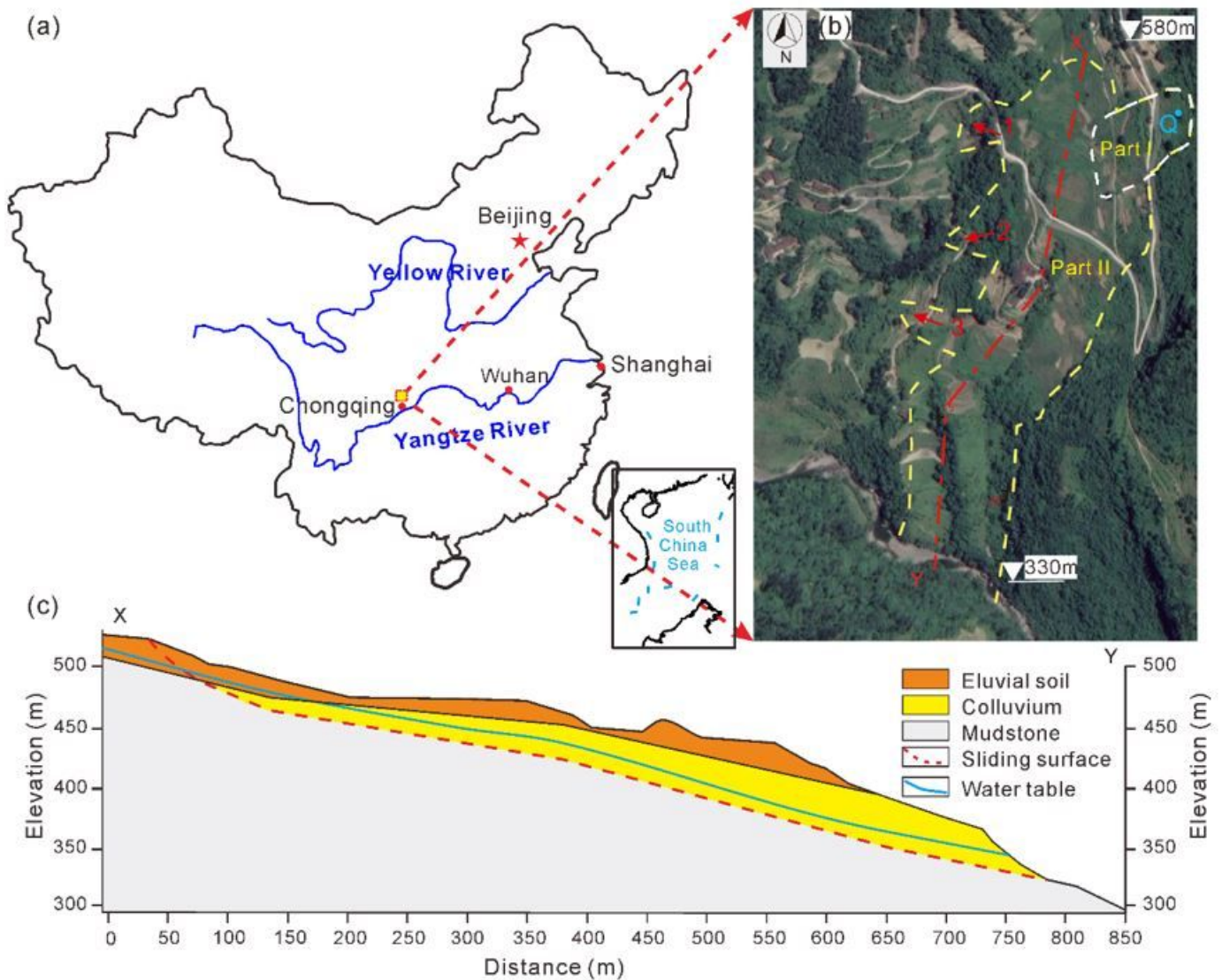


Figure 1

Zhongbao landslide: a) location of the landslide, b) plane view and c) vertical profile after landslide failure Note: The designations employed and the presentation of the material on this map do not imply the expression of any opinion whatsoever on the part of Research Square concerning the legal status of

any country, territory, city or area or of its authorities, or concerning the delimitation of its frontiers or boundaries. This map has been provided by the authors.

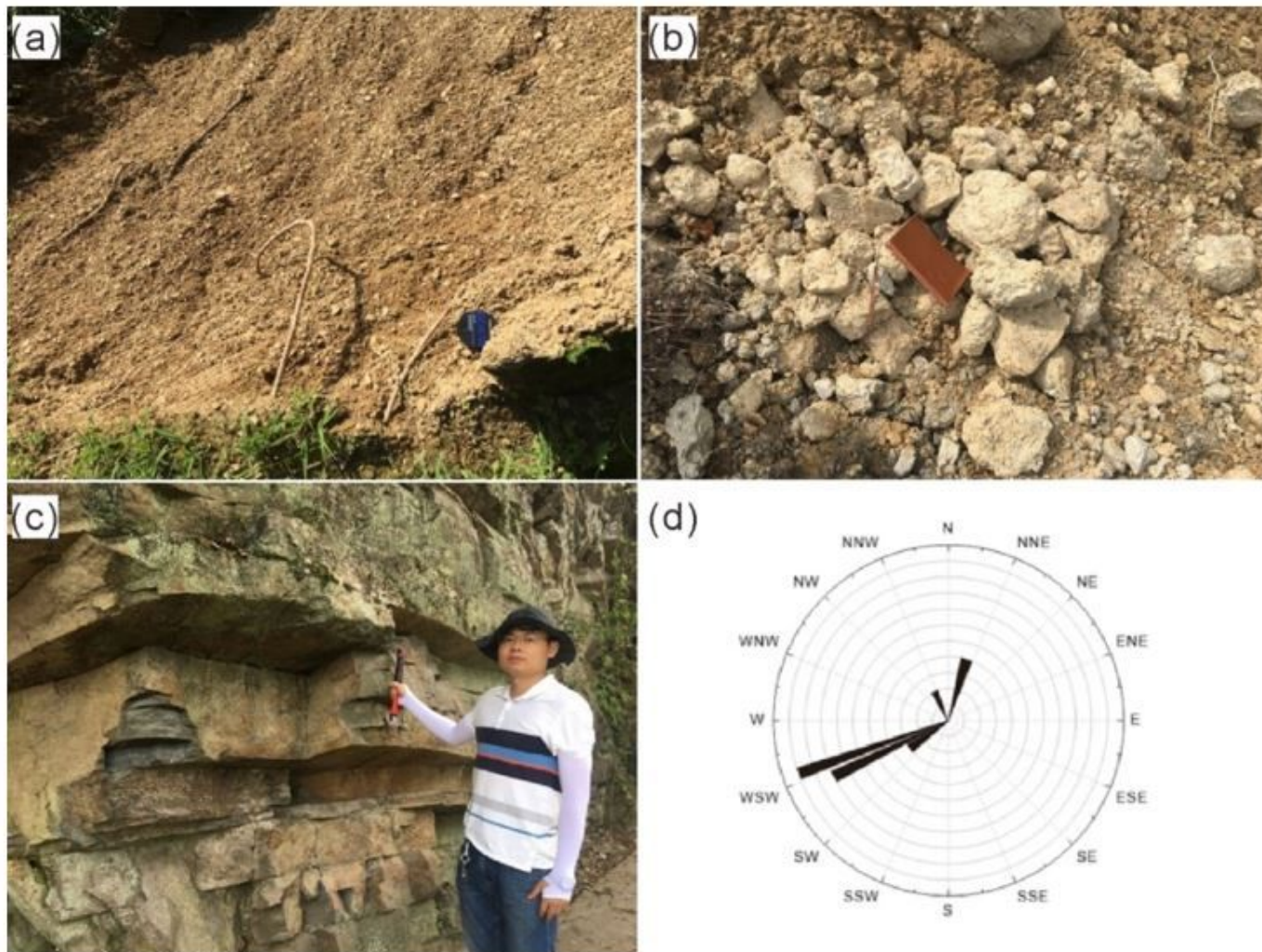


Figure 2

a) Eluvium, b) gravel soil, c) Hanjiadian Formation Shale (S1h) and d) rose diagram of the joints



Figure 3

Monitoring system of the failure landslide and photographs of the devices Note: The designations employed and the presentation of the material on this map do not imply the expression of any opinion whatsoever on the part of Research Square concerning the legal status of any country, territory, city or area or of its authorities, or concerning the delimitation of its frontiers or boundaries. This map has been provided by the authors.

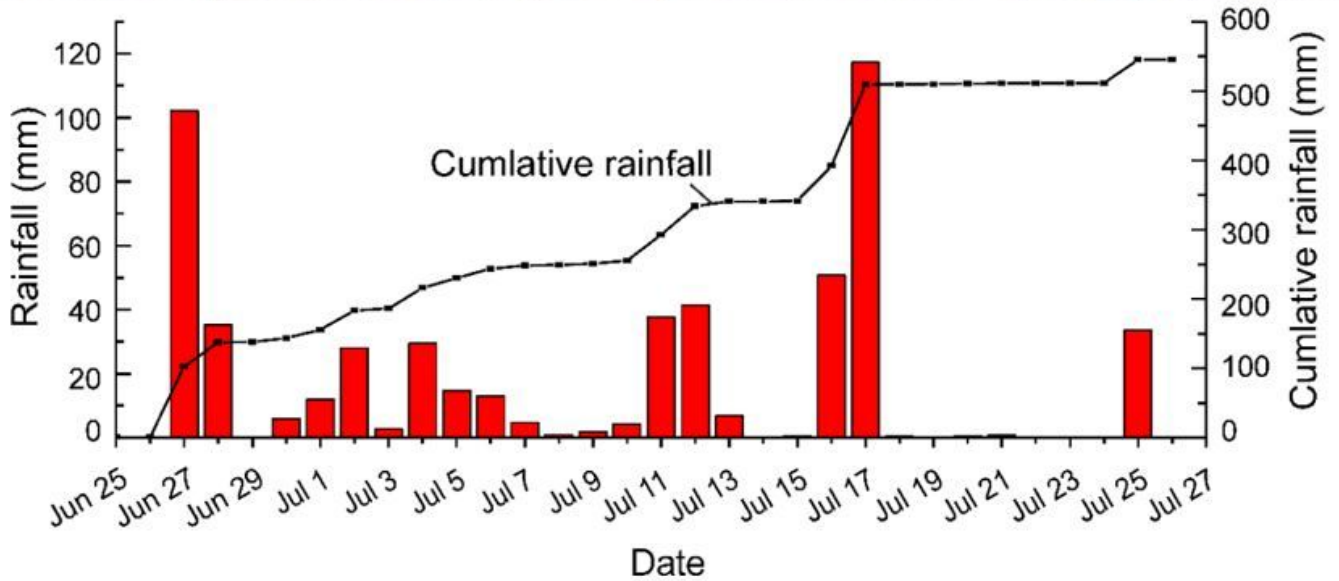
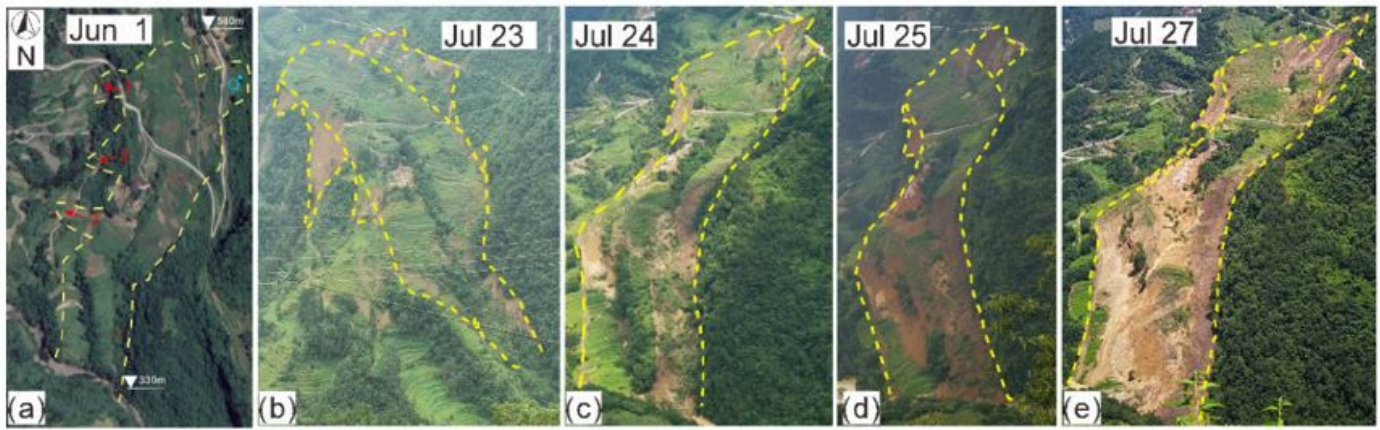


Figure 4

Deformation characteristics and rainfall versus time Note: The designations employed and the presentation of the material on this map do not imply the expression of any opinion whatsoever on the part of Research Square concerning the legal status of any country, territory, city or area or of its authorities, or concerning the delimitation of its frontiers or boundaries. This map has been provided by the authors.

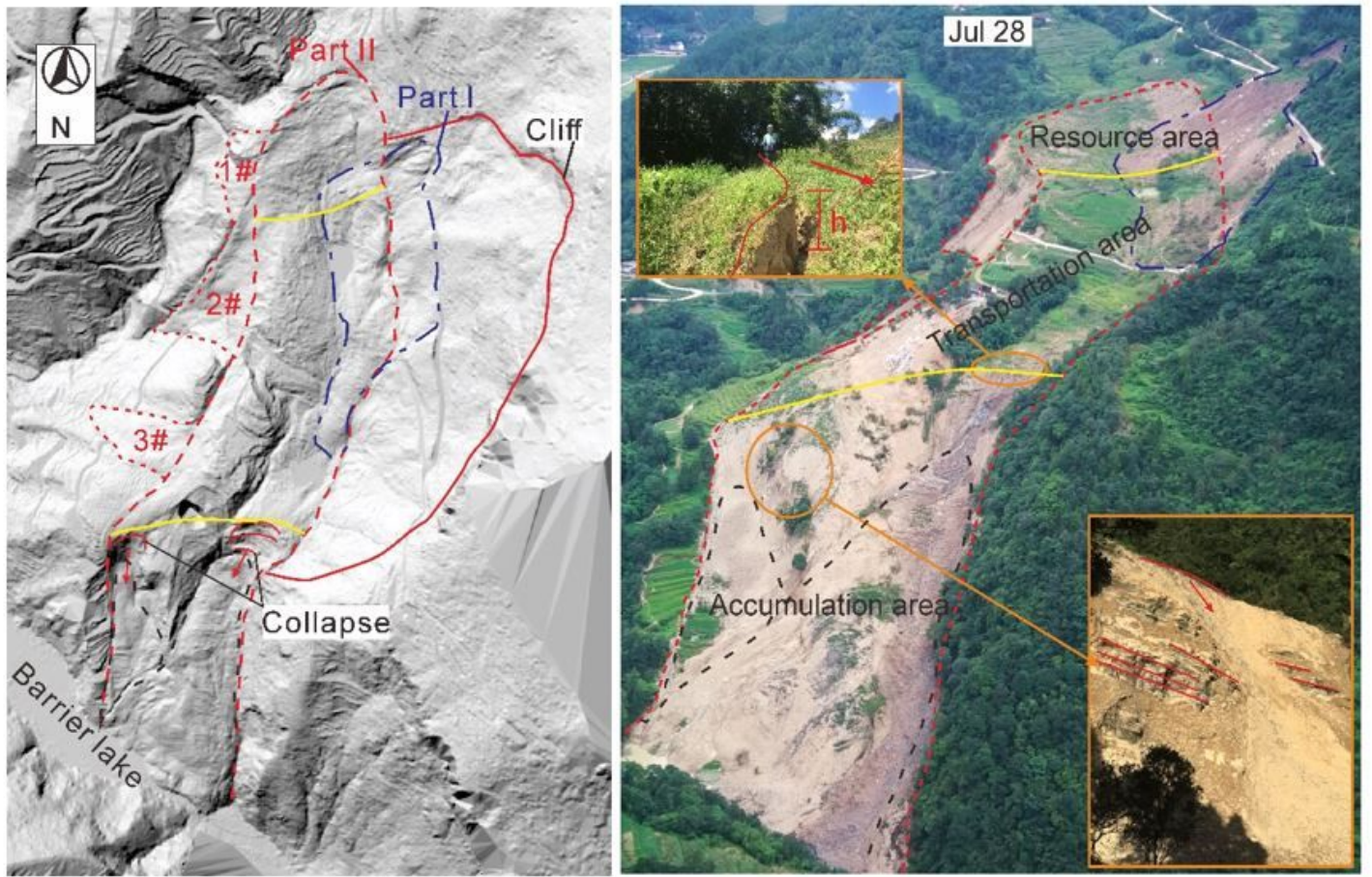


Figure 5

The result of the Airborne Lidar after filter trees. Note the black dashed line is the secondary landslide in the accumulation area. Yellow lines separated the three part (see text). Sub-photographs are the scarplet and local collapse, respectively.

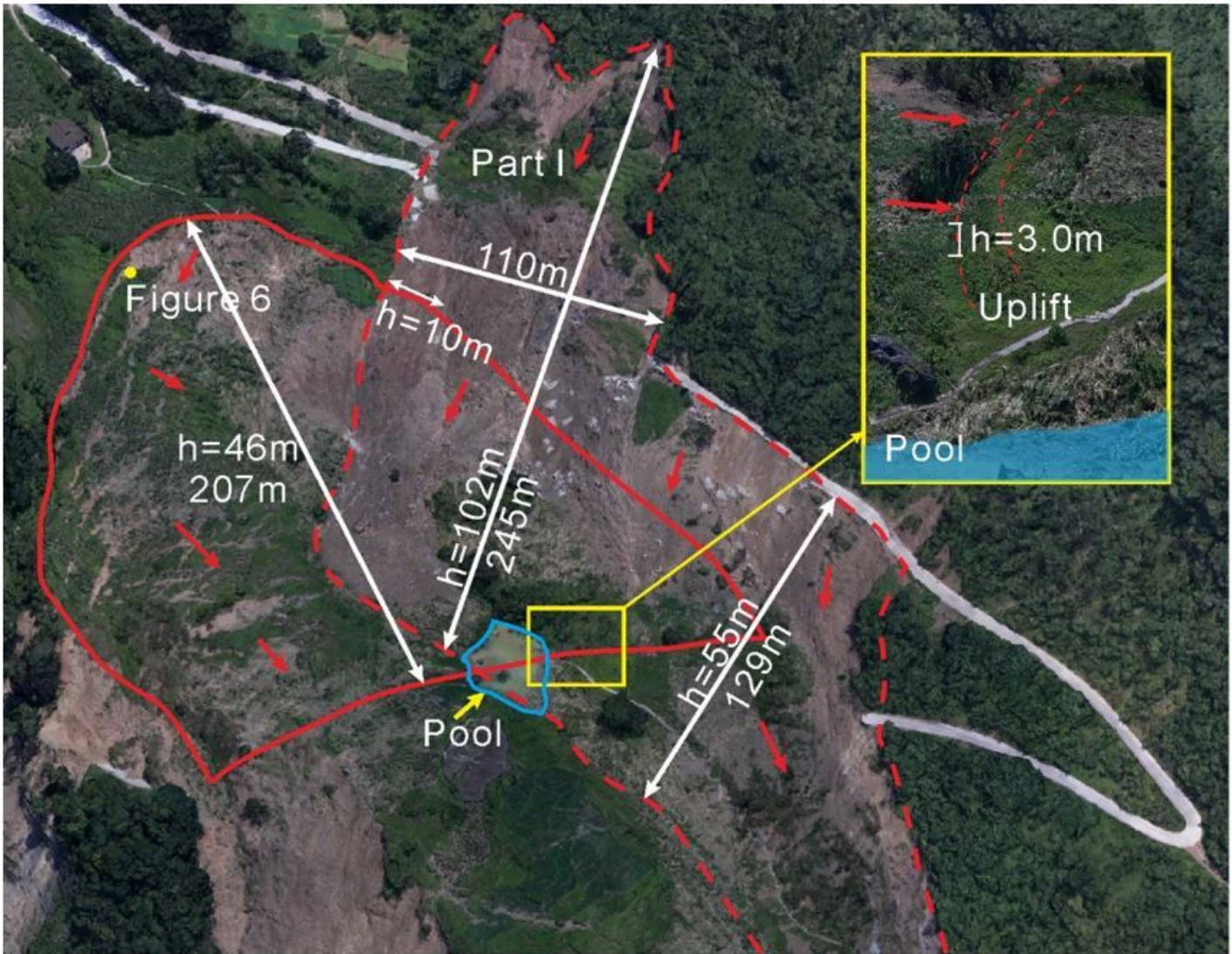


Figure 6

Picture of source area and Part I area. The sub-picture is the uplift zone between source area (left) and transportation area (right). Note, 'h' represents the elevation difference of the landslide area. Note: The designations employed and the presentation of the material on this map do not imply the expression of any opinion whatsoever on the part of Research Square concerning the legal status of any country, territory, city or area or of its authorities, or concerning the delimitation of its frontiers or boundaries. This map has been provided by the authors.



Figure 7

a) Scratch and b) broken rock. See Fig. 3 for the locations of pictures. Note: The designations employed and the presentation of the material on this map do not imply the expression of any opinion whatsoever on the part of Research Square concerning the legal status of any country, territory, city or area or of its authorities, or concerning the delimitation of its frontiers or boundaries. This map has been provided by the authors.



Figure 8

Picture of transportation area. The sub-picture is the village which shows that most of those buildings maintain good integrity. The road also kept good continuity except two sides, even it slid over 90 m. The blue line is pools. Note: The designations employed and the presentation of the material on this map do not imply the expression of any opinion whatsoever on the part of Research Square concerning the legal status of any country, territory, city or area or of its authorities, or concerning the delimitation of its frontiers or boundaries. This map has been provided by the authors.

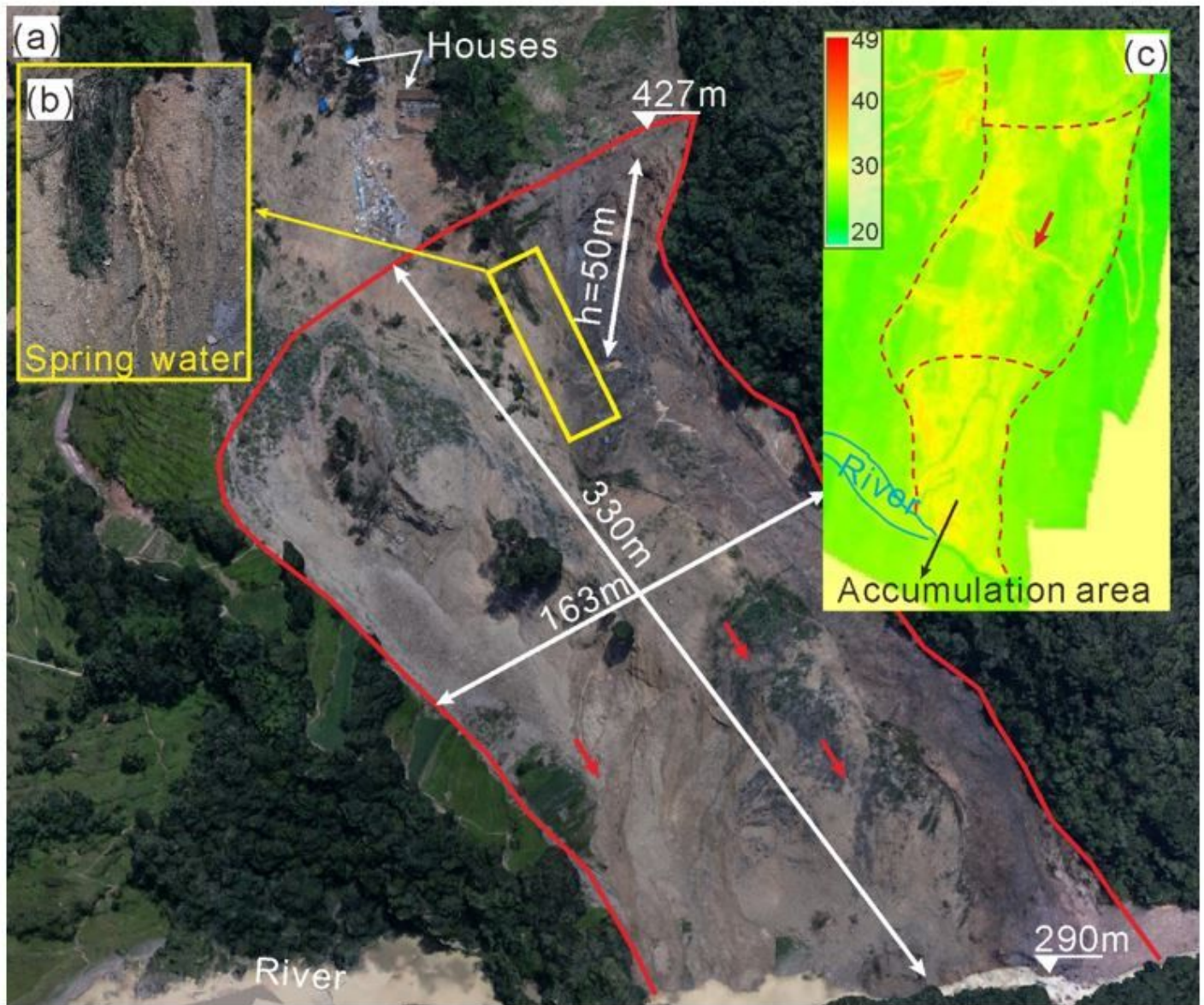


Figure 9

Picture of accumulation area (a), the spring water (b), and the temperature of the landslide surface (c). Note: The designations employed and the presentation of the material on this map do not imply the expression of any opinion whatsoever on the part of Research Square concerning the legal status of any country, territory, city or area or of its authorities, or concerning the delimitation of its frontiers or boundaries. This map has been provided by the authors.

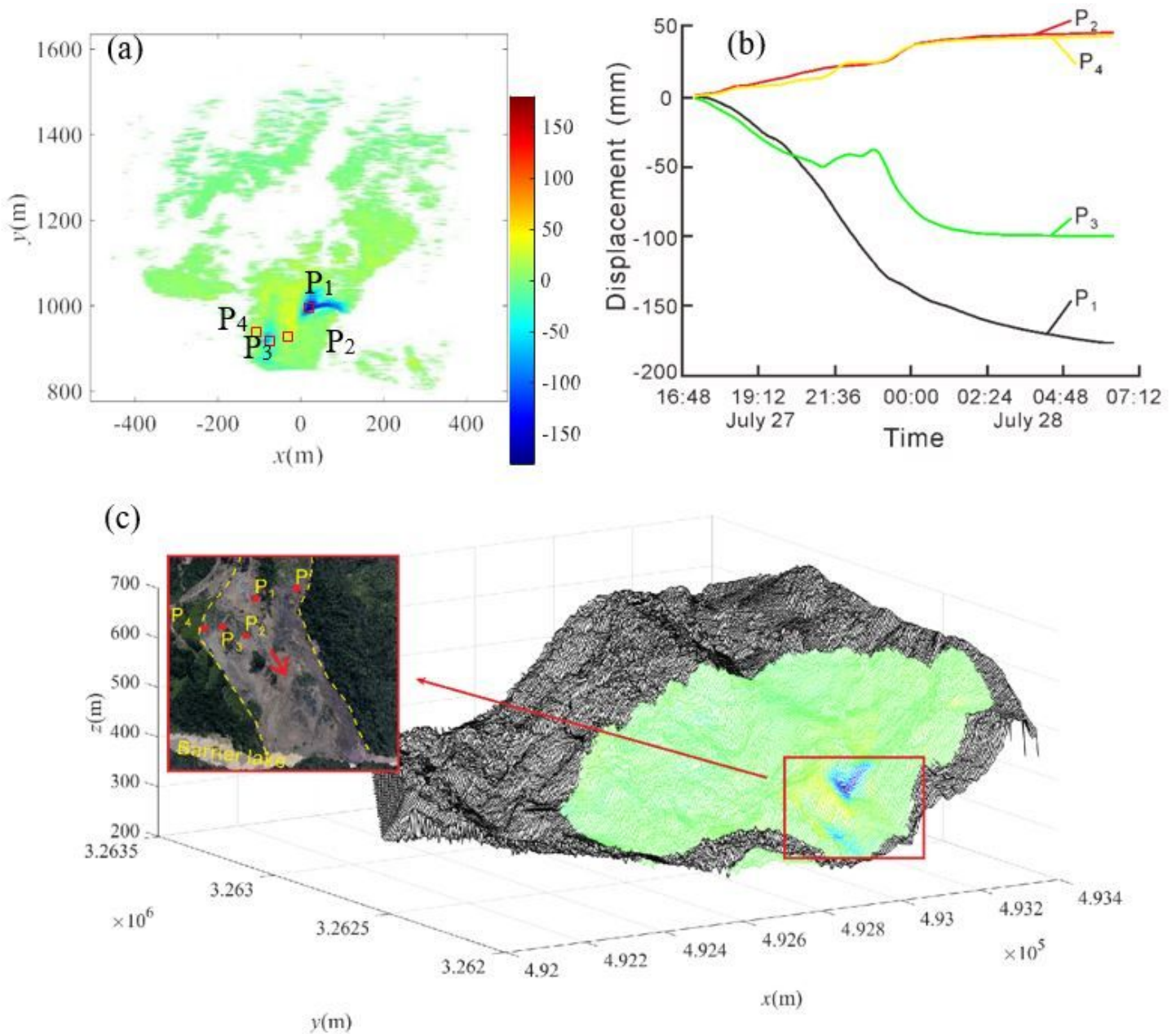


Figure 10

Deformation of the Zhongbao landslide during July 27-28. (a) Accumulative displacement of the landslide surface; (b) the displacements of monitoring points visé time; (c) Three-dimensional topographic map. Note, negative value of the displacement means that the point moves to Radar. Note: The designations employed and the presentation of the material on this map do not imply the expression of any opinion whatsoever on the part of Research Square concerning the legal status of any country, territory, city or area or of its authorities, or concerning the delimitation of its frontiers or boundaries. This map has been provided by the authors.

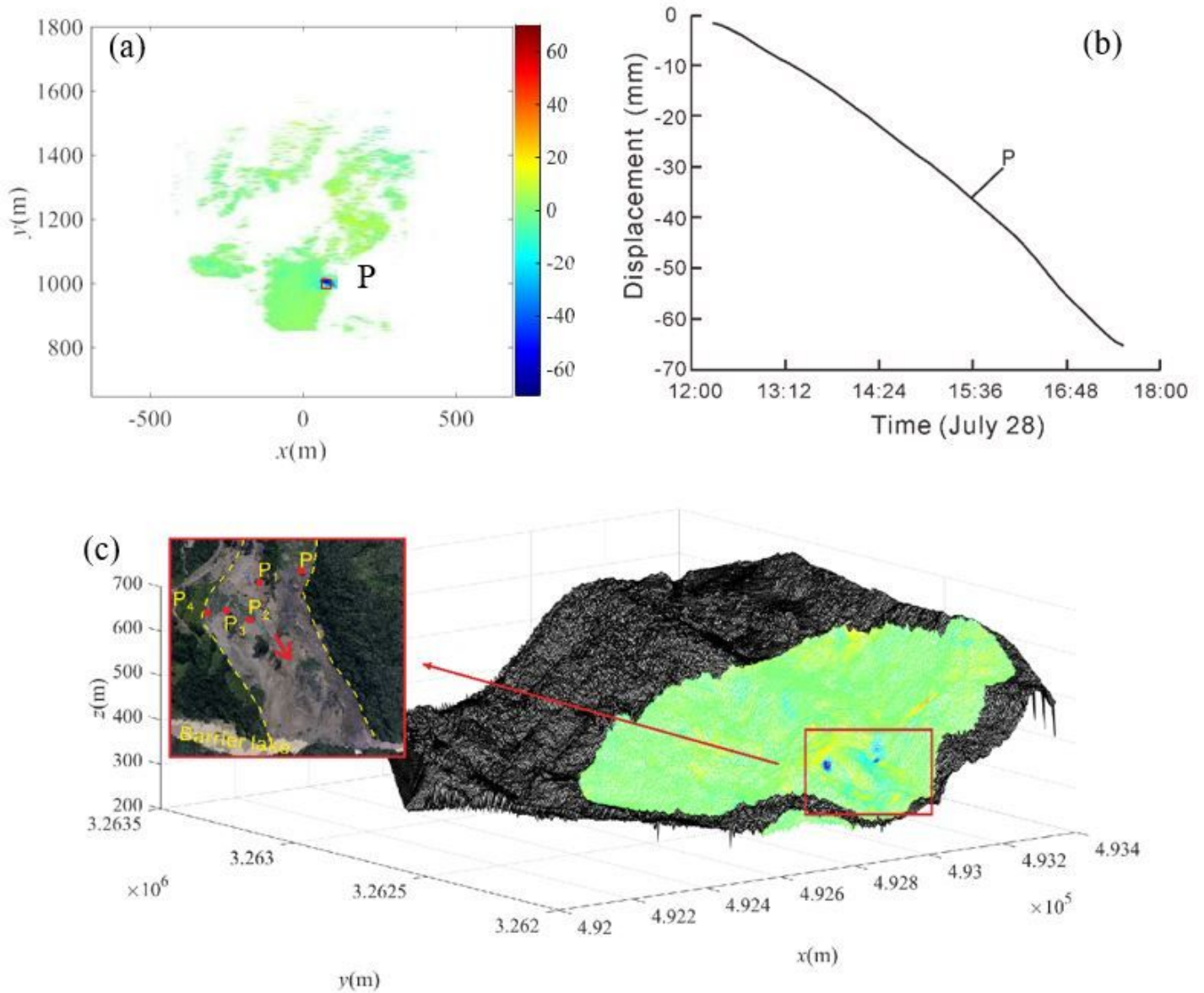


Figure 11

Deformation of the Zhongbao landslide during July 28. (a) Accumulative displacement of the landslide surface; (b) the displacements of monitoring points visé time; (c) Three-dimensional topographic map. Note: The designations employed and the presentation of the material on this map do not imply the expression of any opinion whatsoever on the part of Research Square concerning the legal status of any country, territory, city or area or of its authorities, or concerning the delimitation of its frontiers or boundaries. This map has been provided by the authors.

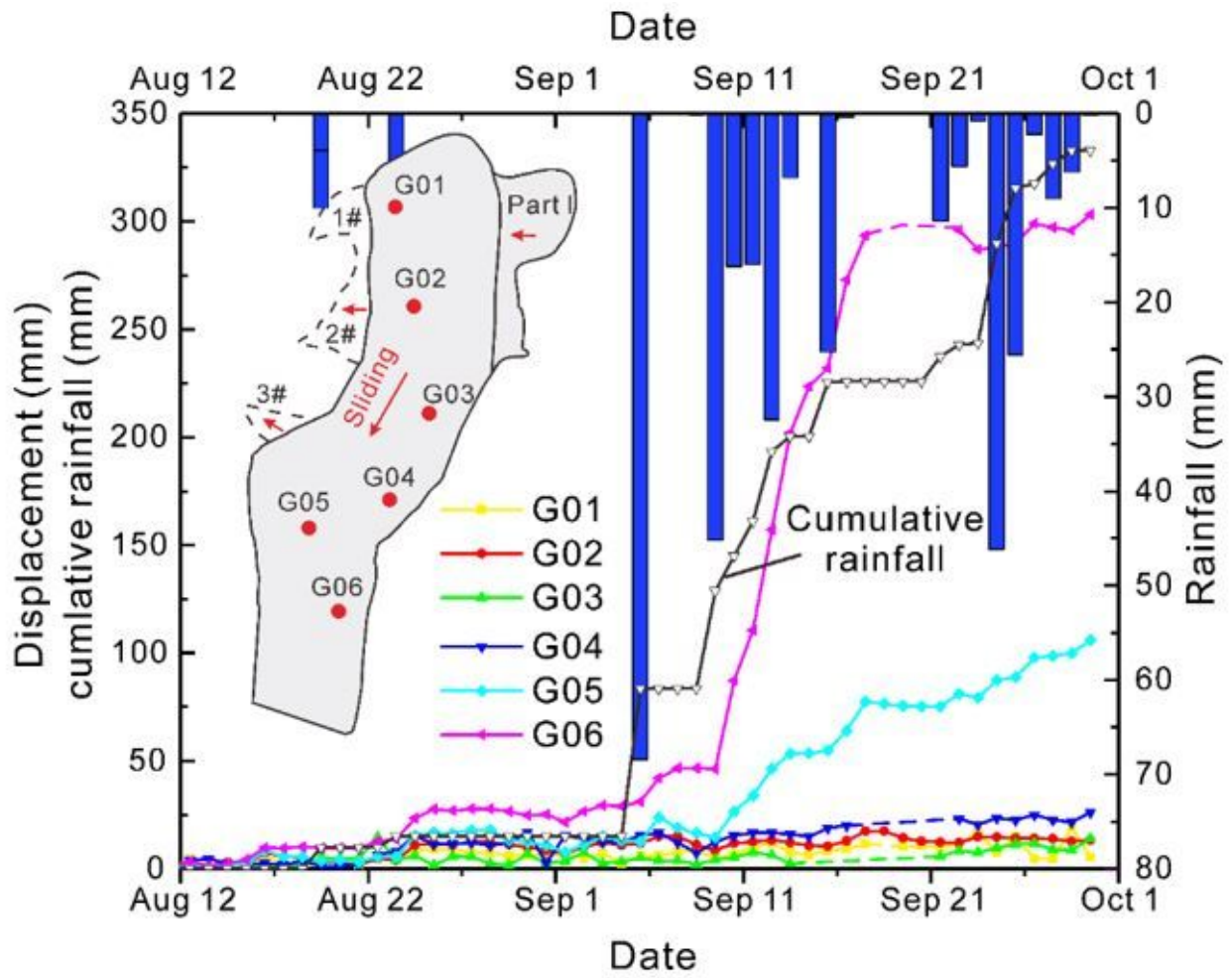


Figure 12

Rainfall cumulative displacement of monitoring points and versus time